

Magnetic Field Properties in High Mass Star Formation from Large to Small Scales - A Statistical Analysis from Polarization Data

Patrick M. Koch¹, Ya-Wen Tang¹ and Paul T. P. Ho^{1,2}

pmkoch@asiaa.sinica.edu.tw

ABSTRACT

Polarization data from high mass star formation regions (W51 e2/e8, Orion BN/KL) are used to derive statistical properties of the plane of sky projected magnetic field. Structure function and auto-correlation function are calculated for observations with various resolutions from the BIMA and SMA interferometers, covering a range in physical scales from ~ 70 mpc to ~ 2.1 mpc. Results for the magnetic field turbulent dispersion, its turbulent to mean field strength ratio and the large-scale polarization angle correlation length are presented as a function of the physical scale at the star formation sites. Power law scaling relations emerge for some of these physical quantities. The turbulent to mean field strength ratio is found to be close to constant over the sampled observing range, with a hint of a decrease toward smaller scales, indicating that the role of magnetic field and turbulence is evolving with physical scale. A statistical method is proposed to separate large and small scale correlations from an initial ensemble of polarization segments. This also leads to a definition of a turbulent polarization angle correlation length.

Subject headings: ISM: clouds — ISM: magnetic fields, polarization, turbulence — ISM: individual (W51 e2/e8, Orion BN/KL) — Methods: statistical

1. Introduction

Giant molecular clouds - the sites of star formation - are threaded by magnetic fields. The exact role of the magnetic field, the nature of turbulence and their interplay are still a matter of debate in the literature. Evidence for a weak magnetic field (super-Alfvénic turbulence) has been presented in e.g. Crutcher et al. (2009); Padoan et al. (2004), whereas support in favor of a strong

¹Academia Sinica, Institute of Astronomy and Astrophysics, Taiwan

²Harvard-Smithsonian Center for Astrophysics, 60 Garden Street, Cambridge, MA 02138, USA

magnetic field (sub-Alfvénic turbulence) controlling the formation and evolution of the molecular cloud is discussed in e.g. Li et al. (2009). Accurate measurements of the magnetic field strength are a key in distinguishing between these two theories.

Different techniques have been employed to measure the magnetic field intensity and structure on various scales. The Zeeman effect provides the only known method of directly measuring magnetic field strengths along the line of sight in a molecular cloud. Generally, it has to rely on strong enough line intensities and also high spectral resolution in order to detect the splitting of spectral lines (Goodman et al. 1989; Crutcher 1999; Troland & Crutcher 2008; Crutcher et al. 2009). Polarization of dust thermal emission at infrared and submillimeter wavelengths provides another method to study magnetic field properties (e.g., Hildebrand et al. 2000). The dust grains are thought to be aligned with their shorter axis parallel to the magnetic field lines, therefore the emitted light appears to be polarized perpendicular to the field lines (Goldreich & Kylafis 1981, 1982; Draine & Weingartner 1996, 1997; Lazarian 2000). Radiative torques are likely to be responsible for the dust alignment (Cho & Lazarian 2005; Lazarian & Hoang 2007). Complementary to Zeeman splitting, dust polarization measurements are probing the plane of sky projected magnetic field direction. However, in order to derive the actual magnetic field strength perpendicular to the line of sight, additional assumptions are needed, as e.g. in the commonly used Chandrasekhar-Fermi (CF) method (Chandrasekhar & Fermi 1953) or in its variations (e.g., Houde et al. 2004; Curran & Chrysostomou 2007).

When applying any of these CF methods, the dispersion in the measured plane of sky polarization is a key parameter. Most studies up to now relied on a magnetic field dispersion measured about a large scale mean field (e.g., Chrysostomou et al. 1994; Lai et al. 2001, 2002; Tang et al. 2009a) or a model field (e.g., Girart et al. 2006; Rao et al. 2009). As noted in Hildebrand et al. (2009), in dense clouds the magnetic field structure might be the combined result from a variety of effects, such as differential rotation, gravitational collapse and expanding HII regions. Consequently, a globally derived dispersion might not reflect the true contribution from magnetohydrodynamic waves and/or turbulence. The recent work by Hildebrand et al. (2009) develops a method based on a dispersion function about local mean magnetic fields. Besides providing a measure for the turbulent dispersion, the method also gives an accurate estimate of the turbulent to mean magnetic field strength ratio. Furthermore, the method is independent of any large scale field model. Hildebrand et al. (2009) discuss applications to the Orion, M17 and DR21 molecular clouds, observed with the Hertz polarimeter at the Caltech Submillimeter Observatory (CSO) with a resolution of $20''$.

Dust polarization observations have been carried out over a range of scales: from the large scale cloud envelope (e.g., Schleuning 1998; Lai et al. 2001) to collapsing cores (e.g., Girart et al. 2006; Tang et al. 2009b). The goal of this paper is to apply and extend the method developed in

Hildebrand et al. (2009) across a range of scales in the same star formation regions.

The paper is organized as follows: Section 2 gives a brief summary of the W51 e2/e8 and Orion BN/KL high mass star formation sites with the results relevant for our analysis. Section 3 defines the structure function and the auto-correlation function with some physical quantities resulting from the statistical analysis. The results are presented in section 4 with a discussion in section 5. Summary and conclusion are given in section 6.

2. Data Set and Source Descriptions

The presented data were obtained with the BIMA and SMA interferometers at wavelengths where the polarization of dust thermal emission is traced. The detailed descriptions of the data analysis and images are given in Lai et al. (2001) for W51 e2/e8 with BIMA, Tang et al. (2009b) for W51 e2/e8 with the SMA, Rao et al. (1998) for Orion BN/KL with BIMA and Tang et al. (2010) for Orion BN/KL with the SMA. Relevant observation numbers are given in Table 1. The re-constructed features depend on the range of uv sampling and weighting. Nevertheless, these data currently provide the highest angular resolution (θ) information on the morphology of the magnetic field in the plane of sky obtained with the emitted polarized light in those star formation sites. They are thus complementary to the earlier analysis with single dish data in Hildebrand et al. (2009) and references therein. This study is part of the program on the SMA¹ (Ho, Moran and Lo 2004) to study the structure of the magnetic field at high spatial resolutions.

2.1. W51 e2/e8

W51 e2/e8 are some of the strongest mm/submm continuum sources in the W51 region. Located at a distance of 7 kpc (Genzel et al. 1981), 1'' is equivalent to ~ 0.03 pc. At a scale of 5 pc, measured at $850\mu\text{m}$ with a resolution $\theta \approx 15''$ with SCUBA on JCMT (Chrysostomou et al. 2002; Matthews et al. 2009), the polarization across the molecular cloud appears to be little organized and not uniform. However, the $350\mu\text{m}$ data, obtained with Hertz on the Caltech Submillimeter Observatory (CSO) show a well-ordered field (Dotson et al. 2010). A comparison of the Hertz and SCUBA data is given in Vaillancourt & Matthews (2008a). Both the e2 and e8 core are unresolved by Hertz and SCUBA. Lai et al. (2001) reported a higher angular resolution ($3''$) polarization map at 1.3 mm obtained with BIMA, which resolved out large-scale structures. In contrast to the larger

¹ The Submillimeter Array is a joint project between the Smithsonian Astrophysical Observatory and the Academia Sinica Institute of Astronomy and Astrophysics, and is funded by the Smithsonian Institution and the Academia Sinica.

scale polarization map, the polarization appears to be more uniform across the envelope at a scale of 0.5 pc, enclosing the sources e2 and e8. In the highest angular resolution map obtained with the SMA at $870 \mu\text{m}$ with $\theta \approx 0''.7$, the polarization patterns appear to be pinched in e2 and also possibly in e8 (Tang et al. 2009b). In the following, where not explicitly written in full, W51 always refers to W51 e2/e8.

2.2. Orion BN/KL

The Orion Molecular Cloud (OMC-1) is one of the closest massive star formation sites. At a distance of 480 pc (Genzel et al. 1981), $1''$ is equal to 2.3 mpc. Source BN/KL is located near the strongest mm continuum emission, where the star formation process is active. Based on single dish polarization measurements obtained with SHARP on the CSO, Vaillancourt et al. (2008b) reported polarization maps observed at 350 and $450 \mu\text{m}$ in the OMC-1 ridge. The revealed magnetic fields appear to be uniform across the dust ridge with effective polarimetric beam sizes of $13''$ at both 350 and $450 \mu\text{m}$. Similar uniform polarization maps have been reported at $100 \mu\text{m}$ by Schleuning (1998) and at $850 \mu\text{m}$ by Vallée & Fiege (2007) with $\theta \approx 15''$. Observed with BIMA at 1.3 mm and 3 mm with θ of $3''.4$ and $7''$, Rao et al. (1998) reported that the polarization appears to change abruptly in the south of the mm continuum peak. With the highest angular resolution achieved with the SMA at $870 \mu\text{m}$, $\theta \sim 1''$, the polarization is consistent with the BIMA detections at 1.3 mm and 3 mm, but the field appears to vary smoothly across the entire core (Tang et al. 2010). In the following, where not explicitly written in full, Orion always refers to Orion BN/KL.

3. Method

This section summarizes how the statistical quantities are derived from the polarization data.

3.1. Structure Function

The polarization position angle (PA) structure function (of second order) is a measure of the mean square deviation in the plane of sky projected magnetic field directions² as a function of scale size. Following the recent work by Hildebrand et al. (2009), we adopt their definition for the

² Assuming the polarization emission to be perpendicular to the magnetic field, the statistics derived from the PA equally apply to the magnetic field.

magnetic field dispersion $\Delta\phi$, which is the square root of the structure function:

$$\langle \Delta\phi^2(l_k) \rangle^{1/2} \equiv \left\{ \frac{1}{N(l_k)} \sum_{l_k \leq r_{ij} < l_{k+1}}^{N(l_k)} (\phi_i(r_i) - \phi_j(r_j))^2 \right\}^{1/2}, \quad (1)$$

where $\phi_i = PA_i$ at position $r_i = (x_i, y_i)$ and $r_{ij} = \sqrt{(x_i - x_j)^2 + (y_i - y_j)^2}$ in each source reference frame with coordinates (x_i, y_i) . $\langle \dots \rangle$ denotes the averaging process over the entire polarization map with respect to r_{ij} for each binning interval l_k . $N(l_k)$ is the number of pairs of PAs with a separation in between the bins l_k and l_{k+1} . All variables are plane of sky projected quantities.

As derived in Hildebrand et al. (2009), assuming the magnetic field B to be composed of a smoothly varying large-scale mean field B_0 and a statistically independent turbulent component B_t , the structure function in the range $\delta < l_k \ll d$ can be written as:

$$\langle \Delta\phi^2(l_k) \rangle_{tot} \simeq b^2 + m^2 l_k^2 + \sigma_M^2(l_k), \quad (2)$$

where δ is the turbulent field correlation length and d is the typical scale for variations in B_0 . $\sigma_M(l_k)$ are the binned error bars resulting from propagating the individual measurement uncertainties. b is interpreted as the scale-independent turbulent field dispersion and ml_k is the linear dispersion term (with slope m) from the large-scale field B_0 . All three contributions, being statistically independent, are added in quadrature. This is basically a first order Taylor expansion of the structure function in the domain where the turbulent field component, B_t , is a small perturbation of a large-scale field B_0 which is smooth on the scale of d . Further following Hildebrand et al. (2009), the ratio between the turbulent and mean magnetic field strength can be calculated by evaluating explicitly the dispersion in the field directions under the assumptions of small perturbations, which results in:

$$\frac{\langle B_t^2 \rangle^{1/2}}{B_0} = \frac{b}{\sqrt{2 - b^2}}. \quad (3)$$

3.2. Auto-Correlation Function

The polarization angle correlation function measures the resemblance or self similarity (correlation with itself) of the projected polarization structure on average as a function of separation. Additionally, it leads to a definition of a characteristic polarization angle correlation length. Whereas the ratio in equation (3) relies on the assumption that the dispersion function can be written as a first order Taylor expansion on the smallest scales, the auto-correlation function with its weighted moments (e.g. correlation length in equation (5)) is independent of such assumptions. In principle, this provides an independent cross-check (see section 5.1) which can probe the assumptions in section 3.1. Furthermore, higher resolution data will allow for an even more detailed modeling

of the field structure without relying on a fit. We calculate the plane of sky projected polarization angle correlation function \mathcal{C} as:

$$\begin{aligned} \langle \mathcal{C}(l_k) \rangle &\equiv \frac{1}{N(l_k)} \sum_{l_k \leq r_{ij} < l_{k+1}}^{N(l_k)} \phi_i(r_i) \cdot \phi_j(r_j) \\ &\equiv \langle \phi(\mathbf{r}) \cdot \phi(\mathbf{r} + l_k) \rangle \end{aligned} \quad (4)$$

where the notation is identical to the one in equation (1). In order to make proper use of the auto-correlation function, one has to assume homogeneous isotropic turbulence, i.e. $\langle \mathcal{C}(l_k) \rangle$ must depend only on the separations r_{ij} . This requires ϕ_i to be rotationally invariant. Whereas this is naturally the case for the structure function, which involves only the square of the difference of the *PA*, the product $\phi_i(r_i) \cdot \phi_j(r_j)$ for the auto-correlation function depends on the reference frame and the definition of the range of the *PA*. The transformation $\phi_i \rightarrow \xi$, $\phi_j \rightarrow \xi - \Delta\phi_{ij}$ expresses all the correlation products with respect to the same position angle $\xi (\neq 0)$, where $\Delta\phi_{ij} = |\phi_i - \phi_j|$. Since $0 \leq \Delta\phi_{ij} \leq 90^\circ$, imposing zero correlation for perpendicular *PA*s fixes $\xi = 90^\circ$. This definition also ensures the correlation coefficients to be in the range between zero and one (*PA*s parallel) when normalized with ξ^2 .

Each observed *PA* will be the result of a superposition of a large-scale (ϕ_0) and a turbulent contribution ($\delta\phi$). Consequently, the correlation function as written in equation (4) contains both contributions mixed. In order to characterize the large-scale polarization the turbulent part needs to be separated. Appendix A gives the details of how to derive a large-scale correlation function, $\langle \mathcal{C}_0(l_k) \rangle$, from an ensemble of measured position angles ϕ , assuming $\phi = \phi_0 + \delta\phi$.

The characteristic large-scale polarization angle correlation length λ_0 is then calculated by integrating the weighted large-scale polarization angle correlation function:

$$\lambda_0 = \frac{\int \langle \phi_0(\mathbf{r}) \cdot \phi_0(\mathbf{r} + l_k) \rangle_r \cdot l_k \, dl_k}{\int \langle \phi_0(\mathbf{r}) \cdot \phi_0(\mathbf{r} + l_k) \rangle_r \, dl_k} \quad (5)$$

where the integration extends over the entire binning range. This is again a plane of sky projected quantity. In the case of a uniform polarization, with all *PA*s being parallel and aligned with a single direction, all the correlation coefficients will be one, independent of scale. The large-scale correlation length λ_0 is then in the middle of the largest and smallest scale, because all the scales are equally weighted (identical correlation) in this case.

We note that the correlation length, being an integrated and weighted measure, is less sensitive to irregularities and incompleteness in the data set (see discussion in section 5.1). In analogy to equation (5), a turbulent polarization angle correlation length λ_t can be estimated, once large-scale and turbulent contributions are separated (Appendix A). A method to calculate the turbulent magnetic field correlation length, based on a generalization of the dispersion function, is derived in Houde et al. (2009).

4. Results

Dispersion function and large-scale auto-correlation function together with turbulent correlation function are presented in Figure 1 and 2 for W51 e2/e8 and Orion BN/KL. For both high mass star formation regions, the polarization data from BIMA (Rao et al. 1998; Lai et al. 2001) and the SMA (Tang et al. 2009b, 2010) are analyzed following section 3. Table 1 summarizes the observations and our findings. The binning intervals l_k are set to integers of the synthesized beams. For elliptical beams, resulting from a non-uniform uv -coverage, the geometrical mean is adopted. Within each binning interval k , dispersion and auto-correlation are evaluated for $l_k \leq r_{ij} < l_{k+1}$. Correlated data points below the synthesized beam resolution are removed. Only PAs with a polarized flux of more than $3\sigma_{\text{Ip}}$, the rms noise of the polarized intensity, are included. Errors of individual PAs are typically in the range of 5° to 10° . The binned error bars ($\sigma_M(l_k)$ in equation (2)) in the Figures 1 and 2 are then determined by propagating the individual errors through the equations (1) and (4). For the dispersion function they are typically around 0.5 or less for the smallest scales. This is due to the sample variance factor from the large number of data points (~ 100 or more pairs of PAs). They grow to a few degrees at the largest scales. Fitting for the turbulent dispersion b is based on a least square fit of equation (2). The small binned error bars are neglected here, which is justified by the possible larger biases as it is discussed in section 5.1.

4.1. W51 e2/e8

The statistical analysis for W51 e2/e8 was performed with three data sets: BIMA (Lai et al. 2001) at 1.3 mm with a resolution of $2''.3$, covering the large-scale structure over $\sim 20''$, and SMA at $870\mu\text{m}$ with a resolution of $0''.7$, separately resolving the regions e2 and e8 over about $4''$ (Tang et al. 2009b). All dispersion functions (structure functions of second order) show an increase over at least the first two bins (Figure 1, left panels). The larger scale BIMA measurement reveals a gentle increase in dispersion with a hint of a plateau at the largest scales (Figure 1, left bottom panel). This is very similar to the results in Hildebrand et al. (2009), obtained with a $20''$ resolution in M17, DR21 Main and OMC-1. The higher resolution SMA observations show a steeper slope over the first two bins, with a dispersion at the smallest scales of about 40° and 55° , compared to about 10° in the BIMA observation. Whereas increase at smaller scales and tendency of a plateau at larger scales are still observed, the higher resolution observations show more irregularities. This is particularly the case for W51 e8.

Following Hildebrand et al. (2009) the turbulent field dispersion b , as defined in equation (2), is obtained from the zero intercept of the fit at scale=0. In order to stay in the linear regime, the first three bins from the BIMA data and only the first two bins from the SMA data are used.

(red solid lines in Figure 1, left panels). The resulting turbulent dispersions around the mean local magnetic field range from $\sim 6^\circ$ to $\sim 54^\circ$, with corresponding turbulent to mean field strength ratios from 0.1 to 0.9 (equation (3)). Higher resolution observations reveal larger values.

The large-scale polarization angle correlation function for the BIMA observation shows a smooth curve as expected from the dispersion (Figure 1, bottom right panel, solid line): a small dispersion at small scales translates into a close correlation at these scales. At the BIMA largest scales, tracing the large-scale polarization variations, the auto-correlation decreases accordingly. The SMA observations of both e2 and e8 show correlations at the shortest scales which are followed by a rather sharp drop and a plateau-like extension. This again reflects the corresponding features in the dispersion functions. Both cores show a secondary peak in the auto-correlation function at larger scales, probably tracing symmetry features in the hourglass-like pinched field morphology. Calculating the characteristic polarization angle correlation length over the maximum scale range, as introduced in equation (5), we find $\lambda_0 = 230$ mpc for the BIMA observation and $\lambda_0 = 73$ mpc and 63 mpc for e2 and e8, respectively. Due to the relatively small field of view sampled in our observations, the values of λ_0 possibly represent lower limits³. This can then also explain why the correlation does not fully vanish at the largest scales.

The same panels in Figure 1 also show the small-scale correlations, separated by the method described in Appendix A. It is apparent that the turbulent correlation function, after an initial sharp drop, is still showing features similar to the large-scale function $\langle \mathcal{C}_0 \rangle$. This is a consequence of the weighting scheme outlined in Appendix A, where even at a larger scale small dispersion values can be accounted for a turbulent correlation with a certain probability. Limiting the turbulent correlation to within the first few bins yields λ_r between 25 and 45 mpc.

4.2. Orion BN/KL

Four data sets with very different resolutions were analyzed for Orion BN/KL: BIMA observations at 3 mm and 1.3 mm with a resolution of $7''$ and $3.''4$ (Rao et al. 1998), and SMA observations at $870\mu\text{m}$ from a combined compact with subcompact, and a compact with extended configuration with resulting synthesized beams of $2.''8$ and $0.''9$ (Tang et al. 2010). The general tendencies found for W51 e2/e8 - increase at smaller scales and plateau-like extension with some irregularities at

³ Additionally, some information on the largest scales might be absent due to the missing zero-spacing in the interferometric observations. However, most of the observations used here contain information from short baselines with lengths comparable to a few antenna diameters, and coherent large-scale structures are apparent in the polarization maps. Correlations on even larger scales - also given the observed trend of decreasing correlation coefficients with larger scales - are therefore likely to add only negligibly to λ_0 .

larger scales for the dispersion function and their analogous features in the auto-correlation function - are still present in Orion BN/KL (Figure 2). However, already the lower resolution BIMA observations, in particular at 1.3 mm, show larger irregularities than the high resolution W51 e2/e8 data. Since they are probing different physical scales at the corresponding source distances (W51 being 14 times further away than Orion), these larger irregularities might simply be due to different morphologies and structures in the magnetic fields. In all cases, the three lowest bins, showing a close to linear increase in dispersion, were again used to fit for the turbulent dispersion b . Values in the range of $\sim 13^\circ$ up to $\sim 33^\circ$ for the highest resolution are found (Table 1). The corresponding turbulent to mean field strength ratios are around 0.2 for the BIMA and ~ 0.4 for the SMA observations. Thus, over about an eight times increase in linear resolution, dispersion and turbulent field contribution increase by about a factor of three and two, respectively.

All the auto-correlation functions have in common a rather sharp drop over the first three or four bins (Figure 2 right panels). With successively higher resolutions, this drop occurs within shorter scale ranges: within about $20''$ and $10''$ for the BIMA observations, and $\sim 8''$ and less than $5''$ for the SMA observations. In all cases the auto-correlation function regains after this first drop, either with a smooth slope (BIMA 3 mm, Figure 2, bottom right panel) or with several peaks. The characteristic large-scale polarization angle correlation length, equation (5), turns out to be in the range of ~ 66 mpc to ~ 15 mpc, which is a change of about a factor of four.

The turbulent correlation function again shows a sharp drop over the first few bins. No satisfactory function was found for the BIMA 1.3 mm observation. This is likely due to the incompleteness of the statistics (only few polarization segments) which the method in Appendix A relies upon. λ_r derived from the first few bins is between 36 and 9 mpc.

5. Discussion

5.1. Validity and Robustness of Approach

Since the high resolution observations are revealing some differences and likely probe a different magnetic field regime (section 5.4), we re-assess here the validity of our approach when deriving the turbulent dispersion and turbulent to mean field strength from equation (2). In order to stay well within the linear range, the derivation in Hildebrand et al. (2009) assumes $\delta < l_k \ll d$. Whereas the turbulent magnetic field correlation length δ is a fundamental limit related to the turbulence dissipation scale and the ambipolar diffusion scale L , the upper limit d , the typical length scale for variations in the large-scale mean field B_0 , depends on the magnetic field under consideration. For the field threading a molecular cloud (envelope), d will be on the order of 100 mpc or more (e.g. envelope in W51 e2/e8). In the case of a collapsing core, the remaining large-scale

field is of the size of the core diameter, which is around 50 mpc for W51 e2 (Tang et al. 2009b). It becomes clear that the allowable interval $\delta < l_k \ll d$ shrinks with higher resolution. Nevertheless, in such a cascading picture, a previously small scale field component becomes the large-scale mean field component at the next higher resolution. This still satisfies the assumptions as long as the resolution is not too high. It should be further stressed that the method in Hildebrand et al. (2009) is entirely independent of a mean field modeling, because of the restriction $l_k \ll d$. Some values of the derived turbulent polarization angle correlation length λ_t (Appendix A) are comparable to the smallest measured scales or even larger. Therefore, $\lambda_t \sim \delta < l_k$ is, strictly speaking, not valid everywhere. Should the correlation length indeed be of the order of 10 mpc, some of our observations are already resolving this scale. In such a case - referring to curve E in Figure 1 in Hildebrand et al. (2009) - the turbulence contribution to the dispersion is probably underestimated because the fitting is done in a range where the turbulence contribution has not yet reached its maximum. The derived turbulent to mean magnetic field strength ratios are then lower limits. We note that the highest resolution SMA observation in Orion (Figure 2 top left panel, $\theta \sim 2.1$ mpc) is close to but not yet resolving the ambipolar diffusion scale L ($L \sim 1$ mpc from Li & Houde (2008); Lazarian et al. (2004)).

In order to probe the robustness of the approach, a threshold test is introduced. *PAs* with a continuum intensity above a certain limit are excluded from the analysis. In the original work by Hildebrand et al. (2009) only data with a magnetic field organization on large scales are analyzed. Our data set additionally contains data where the magnetic field is organized on smaller scales. This is for example the case for the hourglass-like pinched field lines in the collapsing core of W51 e2 where the central pinched field lines correlate with the strongest emission (Tang et al. 2009b). This threshold test addresses a possible concern whether there is a bias toward the strongest emission data. For Orion no relevant change in the dispersion function is found until discarding $\sim 50\%$ of the data ($\sim 70\%$ cut in intensity). In particular, the turbulent dispersion derived from the fit shows a scatter within only $\sim \pm 2^\circ - 3^\circ$, therefore not altering the original results and proofing them to be quite robust. This is verified for all the Orion data sets. Further excluding more than 50% of the data distorts the dispersion function, producing unreliable fits and turbulent dispersion values. The same results hold for W51 as observed with BIMA. The higher resolution observations of W51 e2 and e8 however are found to be a little less robust. For both e2 and e8 a decrease of $\sim -7^\circ$ in the turbulent dispersion is found when excluding up to 30% of the data. Excluding more than 30% of the data leads to unreasonable results. In the case of a collapsing core (like e2 and possibly e8), gravity pulls in the magnetic field lines and presumably affects and dominates turbulence on some scales, bending the field lines on the shortest scales possibly more than what turbulence would do. Removing the strongest intensity data – which are in this case closest to the center of the collapsing core – is likely to reduce a possible gravity induced bias on the shortest scales. The observed decrease in the turbulent dispersion possibly reflects this. In the subsequent Figure 3,

these values are shown with a down-arrow (\downarrow) indicating this possible bias.

Additionally, the dependence on the bin size has been checked. Decreasing the bin size by about 30%-50% of the synthesized beam leaves most of the results practically unchanged, with a typical $\sim 1^\circ$ to 2° down shift in the turbulent dispersion. This results from the denser sampling at the shortest scales which then extends the linear part of the dispersion function toward a slightly shorter scale. This in turn leads to a slightly lower value of the intercept at scale= 0. Whereas oversampling shows little effect, under-sampling with a twice as large synthesized beam significantly biases the analysis toward larger dispersion values. This can be understood from the steep slope over the first few bins. Averaging over large scales then increases the dispersion value. An exception to this conclusion are again W51 e2 and e8. Oversampling by a factor of two reduces the turbulent dispersion to $\sim 15^\circ$. This is possibly due to the same reason as described above for the threshold test: Grouping the few values with a large dispersion in a separate bin will lead to a much lower dispersion for the remaining ones in another bin. Orion, from the BIMA 1.3mm data, shows noticeable effects when the bin size is changed by only 10% to 20%. This is possibly due to the rather irregular dispersion function.

In summary, the tests described above demonstrate that the analysis gives generally robust results with a small scatter. The possible exception is W51 e2 and e8, which might be biased toward too large dispersion values. In the remaining sections, the discussion will be based on the original values, with a reminder of the possible bias where necessary.

The polarization angle correlation function $\langle \mathcal{C}(l_k) \rangle$, being mathematically related to the structure function via $\Delta\phi^2(l_k) \sim 2(\langle \mathcal{C}(0) \rangle - \langle \mathcal{C}(l_k) \rangle)$, reflects the above discussed features analogously. We remark that, although this mathematical connection exists, the presented auto-correlation functions, $\langle \mathcal{C}(l_k) \rangle$ and $\langle \mathcal{C}_0(l_k) \rangle$, are calculated directly from the PAs which provides thus an independent consistency test. Mathematical relation and direct calculation are verified to lead indeed to the same results for $\langle \mathcal{C}(l_k) \rangle$.

For the large-scale correlation function $\langle \mathcal{C}_0(l_k) \rangle$, after separating the small scale turbulence contribution (appendix A), an immediate verification is not possible any more. No reference in the literature was found allowing a direct comparison here with other observations. Technically, the relative errors for the auto-correlation function are smaller than for the dispersion function (less than 1% compared to about 1 to a few percent), as a result of the error propagation of the sum of products compared to the sum of differences.

Finally, we propose here to use the resulting large-scale polarization angle correlation length λ_0 as a quantitative measure for the typical scale d of variation in the ordered polarization structure. The derived values (Table 1) match reasonably well with the above quoted empirical values which are estimated from the polarization maps. Our results are then based on the dispersion function

within $\delta < l_k \ll \lambda_0$. Having a statistical measure for d through the auto-correlation length λ_0 then also verifies the regime where the method based on the dispersion function (section 3.1) can be applied. Since λ_0 is an integrated and weighted measure, threshold test and bin size show only negligible changes. In the course of the tests described above, oversampling and under-sampling by a factor of two give variations in λ_0 of less than 10% for all observations.

5.2. Comparison with Previous Results

Generally, the dispersion functions derived from the present observation set for both W51 e2/e8 and Orion BN/KL are less smooth than those derived from lower resolution single dish observations (Hildebrand et al. 2009; Kirby 2009). We speculate that these irregularities are tracing underlying changes and structures in the magnetic field morphology which become more manifest only at higher resolution (θ), but are smoothed out at lower resolution. The previous larger scale (lower resolution) single dish observations show polarization patterns which extend to such radii where the magnetic field straightens out as the gravitational influence is weak (e.g. OMC-1 in Schleuning (1998) with the Kuiper Airborne Observatory (KAO) at $100\mu\text{m}$ with a resolution of $\sim 35''$ and in Houde et al. (2004) with the Hertz polarimeter at CSO with $\theta \sim 20''$ at $350\mu\text{m}$). M17 SW, observed over a $\sim 6' \times 6'$ field with the KAO shows an overall orderly field configuration with a hint of being pulled into the cloud core by gravitational collapse (Dotson 1996). At the smallest separations, the average change in polarization is around 10° . The sample of 12 Galactic clouds observed with the KAO shows mostly organized large scale fields (Dotson et al. 2000). No dispersion functions were derived for this sample.

Signs of a collapsing cloud in the center, with otherwise mostly straightened field lines, are observed for DR21 Main (Kirby 2009). A smooth dispersion function is found with a dispersion of $\sim 10^\circ$ in the lowest bin and a linear increase to $\sim 25^\circ$ over the next three bins. The one case in which we observe an equally smooth dispersion is W51 observed with BIMA. Similarly to DR21 Main, this observation is tracing the large-scale field envelope⁴, but without yet revealing a collapsing core (Lai et al. 2001). The lowest bin dispersion is again around 10° , then linearly increasing over the next four bins to about 30° (Figure 1 bottom left panel). The single dish (DR21 Main with CSO, spatial resolution ~ 0.2 pc) and interferometer (W51 with BIMA, spatial resolution ~ 0.1 pc) seem to be revealing comparable structures and dispersion values around 10° here. Such dispersion values then lead to a turbulent to mean field strength ratio of 0.1 to 0.15.

⁴ The smaller scale field structures are likely to be beam-diluted because of averaging in the plane of sky, but not along the line of sight. In the opposite case, higher angular resolution data, e.g with the SMA, would not be able to reveal coherent structures on smaller scales.

These numbers are also consistent with the values reported recently in Hildebrand et al. (2009) for OMC-1 and M17. Our remaining data are directly probing the collapsing cores with clearly pinched magnetic field lines for W51 (see Figure 6 in Tang et al. (2009b)) and a wrapped toroidal-like structure in Orion (Tang et al. 2010). For this different physical regime - although previous observations exist (Girart et al. 2006) - no analysis based on a dispersion function was performed which would allow a comparison. A turbulent to magnetic energy ratio of ~ 0.02 (turbulent to magnetic field strength ratio ~ 0.14) is derived by Girart et al. (2006) based on a remaining mean dispersion after fitting a parabolic function to the field morphology.

A further major difference between our data set (except W51 with BIMA) and the above cited previous works is the steeper slope (section 5.3, Table 1) over the first two or three bins. The dispersion increases typically by 20° to 30° or even more, compared to $\sim 10^\circ$ in the above cited cases. The values at the first bins are already around 20° or 30° whereas the other cases show numbers around 10° or less. The corresponding turbulent to mean field strength ratios are then in the range of ~ 0.2 to 0.54 .

Different methods, also aiming at constraining the turbulent to mean field ratio but not going through a structure function, have been explored by several authors. Based on an average *PA* dispersion $\delta\phi < 13^\circ$, a turbulent to magnetic field energy ratio has been estimated in Lai et al. (2002) for NGC 2024 FIR 5 in the Orion B Giant Molecular cloud. Their energy ratio (< 0.14) corresponds to a turbulent to mean field strength ratio < 0.37 . The ratio of mass-to-flux, M/Φ , is evaluated in Troland & Crutcher (2008) for a set of 34 dark cloud cores (~ 0.01 pc) from OH Zeeman observations with the Arecibo telescope. Their average ratio of turbulent to magnetic energy is ~ 2 , the turbulent to mean field ratio therefore about 1.4. Part of these data, in combination with GBT observations of the cloud envelope (~ 1 pc), were then used to provide support for a super-Alfvénic (weak magnetic field) turbulence model (Crutcher et al. 2009). Average dispersion values (not dispersion functions) around a mean magnetic field direction were also derived in Myers & Goodman (1991) from optical polarimetry and in Novak et al. (2009) from submillimeter polarization. In the latter work the authors found a turbulent to mean field ratio in the range between 2.0 (intermediate field) and 0.52 (strong field) compatible with their observations.

5.3. Comparison with Numerical Simulations

The turbulent to magnetic field energy ratio is also investigated through numerical simulations. Ostriker et al. (2001) analyzed the time evolution in a model cloud simulation with three different magnetic field strengths (strong, medium and weak field with $\beta = c_s^2/B_0/(4\pi\bar{\rho}) = 0.01, 0.1$ and 1 , respectively), but an identical initial turbulent velocity field. The perturbed magnetic field energy reaches a maximum at about 0.1 - 0.2 times the Alfvénic crossing where it

accounts for about 20 - 50% of the total turbulent energy (kinetic energy and perturbed magnetic energy together). In their projected snapshot only the strong field model ($B_0 = 14 \mu\text{G}$) leaves significantly correlated ordered polarization segments with a perturbed to mean magnetic energy $\beta_{turb} = \delta B^2 / B_0^2 \approx 0.27$. This corresponds to a turbulent to mean field strength ratio of about 0.52. Although this is comparable to the numbers of our higher resolution observations around collapsing cores, it is not obvious to match their snapshot in time evolution within our sequence of low and high resolution data.

On the other hand, recent simulation results with supersonic and super-Alfvénic turbulence, in combination with simulated Zeeman measurements, find $\beta_{turb} \gtrsim 1$ for cores with a radius $\sim 0.2 - 0.8$ pc (Luntila et al. 2009). This seems to be in favor of the turbulent to magnetic energy ratios observed in Troland & Crutcher (2008), who found an average $\bar{\beta}_{turb} \approx 2$ for comparable core sizes and source distances. These findings support a star formation theory with super-Alfvénic turbulence.

Related to β_{turb} , PA structure functions (of second order), $\Delta\phi^2$, are analyzed in Falceta-Gonçalves et al. (2008) with the goal of discriminating between sub/supersonic and sub/super-Alfvénic models. Independent of the magnetic field orientation with respect to the line of sight, sub-Alfvénic models tend to have a power law index $\alpha \sim 0.5$, $\Delta\phi^2(l_k) \sim l_k^\alpha$, whereas super-Alfvénic models show a flatter slope with $\alpha \sim 0.3$. For the set of our observations, α (derived from the first two bins for W51 and three bins for Orion, Table 1) is in the range of 0.3 to 3.2. Although this is closer to sub-Alfvénic models, the rather steep slopes in our structure functions followed by a plateau make a direct comparison with the smoother structure functions in Falceta-Gonçalves et al. (2008) not obvious.

In summary, numerical simulations provide results for the turbulent to magnetic field energy ratio and the slope of the polarization structure function for a series of different models. Some are in agreement with our findings. For a detailed comparison, the difficulty lies in matching observational resolution and star formation stage with the model time evolution in the simulation.

5.4. Dependence on Physical Scale

The angular resolutions obtained from the BIMA and SMA observations vary by about a factor of ten, spanning a range in physical scales at the source distances from ~ 70 mpc to ~ 2.1 mpc (Table 1). As discussed in section 4, the resulting dispersion functions (and auto-correlation functions) show some common tendencies but differ in their detailed characteristics and numbers. Here, we address the question whether the subsequently higher resolution observations reveal a dependence on physical scale. This question is also motivated by the observed polarization maps where

an envelope on the largest scales (BIMA, Lai et al. (2001)) and two collapsing cores with a possible hourglass-like magnetic field morphology on the smallest scales (SMA, Figure 6 in Tang et al. (2009b)) are found in the case of W51 e2/e8. For Orion, the lowest resolution BIMA data and the highest resolution SMA data again reveal very different magnetic field structures. Consequently, we argue that these polarization observations are indeed probing different regimes in the star formation process. The fact that increasingly higher resolutions still reveal detectable local coherent structures, very likely means that large-scale structures are smooth enough for the local structures to be distinguishable. This must hold true for both along and across the line of sight, because otherwise features would be washed out.

Figure 3, top panel, shows the tendencies for the turbulent to mean field strength ratio as a function of the physical scales, as derived from the Figures 1 and 2. As relevant physical scale the synthesized beam resolution is assumed. In addition to the BIMA and SMA data set, the lower resolution data from Hildebrand et al. (2009) for Orion, DR21 and M17 are also added. Over the observed scale range (~ 70 mpc to ~ 2.1 mpc), the turbulent to mean field strength ratio increases with smaller scale by about a factor of ten.

Further investigating this apparent dependence on physical scale in the top panel in Figure 3, we discuss a possible beam resolution effect. Houde et al. (2009), in an expansion on the work in Hildebrand et al. (2009), considered the signal integration aspect in their analysis. They find that the turbulent component of the dispersion function at scale zero, $b^2(0)$, is then the square of the turbulent to large-scale magnetic field strength divided by the number of independent turbulent cells N probed by the observation: $b^2(0) = \langle B_t^2 \rangle / B_0^2 \cdot 1/N$. As further derived, N is directly a function of the beam size and can be written as $N = \frac{(\delta^2 + 2W^2)\Delta'}{\sqrt{2\pi}\delta^3}$, where δ is the turbulent field correlation length, Δ' is the effective depth of the molecular cloud along the line of sight and W is the beam radius. The equation for N in Houde et al. (2009) is derived assuming a (circular) Gaussian beam and Gaussian turbulent auto-correlation functions. For a given source, the smaller the beam size, the smaller N will be, and the bigger b will be if the ratio $\langle B_t^2 \rangle^{1/2} / B_0$ remains constant, or if at least $1/\sqrt{N}$ grows faster than $\langle B_t^2 \rangle^{1/2} / B_0$ decreases. Different beam sizes can therefore mimic a trend in the turbulent to mean field ratio. The top panel in Figure 3 apparently confirms this expectation. In the following we aim at revising the top panel in Figure 3 by taking into account the beam resolution effect, in order to reveal the net change in the turbulence to mean field strength ratio over scale. Starting from equation (44) in Houde et al. (2009), the scale independent term describes the intercept at scale zero in their Figure 2. This is equivalent to our dispersion at scale zero, but with an additional factor containing the beam integration effect. We, therefore, rewrite the turbulent to mean magnetic field ratio as: $\langle B_t^2 \rangle^{1/2} / B_0 = \sqrt{N} / \sqrt{2} \cdot \langle \Delta\phi^2 \rangle_{l=0}^{1/2}$, where $\langle \Delta\phi^2 \rangle_{l=0}^{1/2}$ is the turbulent dispersion derived from our fitting results in Figure 1 and 2. Δ' is approximated with the size of the most extended detected structure, which is roughly the size of the maps in the SMA and BIMA observations. δ (≈ 16 mpc) is adopted from Houde et al.

(2009) for Orion. The beam radius W is derived from the synthesized beams of our SMA and BIMA observations. The estimated number of turbulent cells is listed in Table 1. Figure 3, middle panel, shows the resulting beam corrected turbulent to mean magnetic field strength ratios. After correction, both Orion and W51 show a close to constant ratio over scale, with a slight trend of a decreasing ratio toward smaller scales. Whereas the ratios for Orion are in the range between 0.30 and 0.44, the ratios for W51 (0.7 to 1.27) are around the equipartition limit of turbulent and magnetic field strength. This might be an indication that the role of turbulence and magnetic field changes over scale. In the case of W51, there is possibly a transition from a turbulence dominated to a magnetic field dominated scenario.

Taking into account the beam integration modifies the picture first presented in the top panel. Differences in measured values of $\langle \Delta\phi^2 \rangle_{l=0}^{1/2}$ can result from a combination of a beam integration effect and a variable turbulent to mean field ratio. Both contributions can vary in their significance with scale. Correcting for the beam integration effect reveals the net change over scale in the turbulent to mean field ratio. The beam correction ($\sim \sqrt{N}$) is of importance for lower resolution (larger beam) observations, but becomes less important for higher resolution observations approaching the turbulent cell size. Intuitively, one might expect a turbulent to mean field strength ratio which decreases with smaller scale as the turbulence dissipation scale is approached. The observed trend seems to be in support of this, revealing the beginning of a slight decrease in the ratio. An even higher resolution observation at the mpc scale or smaller might then reveal a breakpoint (turn over) in the scaling. On the other hand, the panels in Figure 3 only display a ratio. It is still possible that the turbulent field strength increases with smaller scale, but at a slower rate than the mean field strength. A power law, $\propto l^\gamma$, is fit to the Orion and W51 data. Table 2 summarizes the results for both the uncorrected and the beam corrected scalings.

We finally remark that there is some uncertainty left in the beam correction due to our approximation for Δ' . Should the detected cores have structures along the line of sight which significantly differ from the detected extension across the plane of sky, the number of turbulent cells N could vary. Underestimating N by a factor of two would change the ratio by $\sqrt{2}$. In order to align Orion and W51, N would need to be underestimated or overestimated, respectively, by about a factor of four. Similarly, a correlation length δ twice as large as in Orion would reduce the ratios for W51 to approximately the ones found for Orion. However, remaining uncertainties in both Δ' and δ do not change the slope of the scaling, unless they significantly vary with resolution. Thus, within these uncertainties Orion and W51 both show indications of a decrease in the turbulent to mean field strength ratio over scale, but with a difference in scale specific ratios possibly reflecting the source environment.

The scaling of the large-scale polarization angle correlation length λ_0 shows a close to straight line (Figure 3, bottom panel), with only a small difference between W51 and Orion. λ_0 decreases

by about a factor of fifteen over the sampled physical scales. We remark that the presented values for λ_0 are possibly lower limits, because of the relatively small fields of view sampled in our observations. Since λ_0 is a normalized measure, equation (5), beam integration effects are likely to cancel out, unless they additionally depend on the spatial scale l_k . The turbulent correlation length λ_t is presumably independent of scale. This is not fully verified from our data set (Figure 3, bottom panel). In some cases this is due to incomplete turbulence statistics, which then do not allow to set a reliable cut off criteria. Additionally, a certain beam integration effect is probably left in $\mathcal{D}(\Delta\phi_{k=1})$, equation (8), which leads to broader or narrower turbulence distributions. This again affects the cut off criteria through μ_Δ (Appendix A). For comparison, a turbulent magnetic field correlation length of ≈ 16 mpc is derived in Houde et al. (2009) for OMC-1.

6. Summary and Conclusion

A set of interferometric polarization observations with resolutions in the range between $7''$ and $0.7''$ (~ 70 mpc to ~ 2.1 mpc) is analyzed to derive statistical properties of magnetic field and turbulence from large to small scales during the star formation process. Our data set covers structures from the large-scale cloud envelope to the collapsing cores. The highest resolution data are close to the expected ambipolar diffusion scale (~ 1 mpc). We apply and expand the method developed recently in Hildebrand et al. (2009). The main results are:

1. The turbulent field dispersion shows a steeper slope and larger values at the shortest scales with increasing resolution. Accordingly, the resulting turbulent to mean magnetic field strength ratio increases with smaller scale over the entire range in physical resolution. This is without taking into account a beam integration aspect, and is in agreement with earlier theoretical expectations.
2. The sequence of low and high resolution observations does not only zoom in onto the same magnetic field structure, but it is probing different morphologies and different stages in the star formation process. This is also supported by the polarization maps. When taking into account a beam integration aspect, both Orion and W51 show a close to constant turbulent to mean field strength ratio over scale, with a slight trend of a decreasing ratio toward smaller scales. Whereas the ratios for Orion are in the range between 0.30 and 0.44, the ratios for W51 (0.7 to 1.27) are around the equipartition limit of turbulent and magnetic field strength. This might be an indication that the role of turbulence and magnetic field changes over scale. In the case of W51, there is possibly a transition from a turbulence dominated to a magnetic field dominated scenario. Our observation set therefore also provides information for the time and spatial evolution of these quantities during the star formation process.

3. Based on the polarization angle correlation function a characteristic large-scale correlation length λ_0 is defined. This can be used as a quantitative criterion to define the scale over which the mean polarization structure varies. λ_0 decreases with higher resolution. Additionally, starting from an ensemble of measured polarization position angles, a method is proposed to separate statistically large-scale from turbulent contributions. This leads to a definition of a turbulent correlation length λ_r .

The authors wish to thank the referees, Roger H. Hildebrand, Martin Houde and John E. Vaillancourt for their comments and explanations which provided important further insight.

A. Polarization Angle Correlation Function

An observed position angle $PA_i = \phi_i$ is the superposition of a large-scale polarization structure and a smaller scale turbulent component. Consequently, a correlation length directly derived from a measured ensemble of ϕ_i contains both small scale and large-scale correlations mixed. In order to calculate a large-scale (mean) polarization angle correlation length separately, one needs to isolate the mean contribution ϕ_{i0} and the turbulent contribution $\delta\phi_i$. In general, this will not be possible for a single or only a few PA s, unless one makes very specific assumptions as, e.g. a given uniform magnetic field direction. However, it is, as outlined in the following, possible to separate the two contributions in a statistical way.

Splitting each PA_i into a large-scale and turbulent part, $\phi_i = \phi_{i0} + \delta\phi_i$, the correlation product for a scale k is written as

$$\sum \phi_i \cdot \phi_j \sim \sum \phi_{i0} \cdot \phi_{j0} + 2 \sum \phi_{i0} \cdot \delta\phi_j + \sum \delta\phi_i \cdot \delta\phi_j, \quad (6)$$

where the mixed correlations $\phi_{i0} \cdot \delta\phi_j$ and $\phi_{j0} \cdot \delta\phi_i$ are set identical when evaluated within the same scale range. The summation extends over $l_k \leq r_{ij} \leq l_{k+1}$ where $r_{ij} = \sqrt{(x_i - x_j)^2 + (y_i - y_j)^2}$ with coordinates (x_i, y_i) for the position angle ϕ_i . The normalization factors are omitted here, and reintroduced later (therefore the sign ' \sim '). Since observationally only ϕ_i is accessible and we wish to isolate $\sum \phi_{i0} \cdot \phi_{j0}$, we replace $\phi_{i0} = \phi_i - \delta\phi_i$ in the mixed correlation, which leads to:

$$\sum \phi_{i0} \cdot \phi_{j0} \sim \sum \phi_i \cdot \phi_j - 2 \sum \phi_i \cdot \delta\phi_j + \sum \delta\phi_i \cdot \delta\phi_j. \quad (7)$$

In order to further proceed, the turbulent contribution $\delta\phi$ needs to be quantified. Although $\delta\phi_i$ is not directly observable for an individual position angle ϕ_i , its distribution $\mathcal{D}(\delta\phi)$ can be constructed. At the smallest observable scale $k = 1$, the difference in two position angles, $\Delta\phi_{ij} = \phi_i - \phi_j$, is mostly reflecting the difference in their turbulent contributions. This is similar to the turbulent

dispersion value which is derived by extrapolating from the smallest scales to the intercept at scale $k = 0$ (section 3.1 and Hildebrand et al. (2009)), with the difference that $\Delta\phi_{ij}$ can be positive or negative. The turbulent distribution $\mathcal{D}(\delta\phi)$ can then be constructed as

$$\mathcal{D}(\delta\phi) = \frac{1}{2} \cdot \frac{b}{\langle \Delta\phi^2 \rangle_{k=1}^{1/2}} \cdot \mathcal{D}(\Delta\phi_{k=1}) \quad (8)$$

where the distribution of $\Delta\phi_{k=1}$ is evaluated from the derived differences in position angles at the smallest scale $k = 1$, and the factor $1/2$ results from assigning half of the difference as turbulent contribution to each of the two PAs. The additional factor $b/\langle \Delta\phi^2 \rangle_{k=1}^{1/2}$ down-weights the measured differences at scale $k = 1$ to the limiting scale $k = 0$, based on the result from the fit for the turbulent dispersion function (section 3.1).

Typically, the turbulence distribution $\mathcal{D}(\delta\phi)$ is expected to be Gaussian around zero. This further means that for a large enough, statistically complete sample, the second term on the right hand side of equation (7) will vanish due to the symmetry of $\mathcal{D}(\delta\phi)$. In order to verify this, the mixed term, $\sum \phi_i \cdot \delta\phi_j$, is calculated by randomly choosing a $\delta\phi_j$ value from $\mathcal{D}(\delta\phi)$. Except for the smallest scale, there are fewer correlation products than sample values $\delta\phi_j$ in $\mathcal{D}(\delta\phi)$, and the mixed term will therefore typically not converge to zero. This statistical sampling limitation can be overcome by repeating the calculation and averaging the results. Typically, for 100 runs or more the results converge and then really probe the statistical completeness of the turbulence distribution. Figure 4 illustrates this for the case of W51 observed with BIMA: $\mathcal{D}(\delta\phi)$, top left panel, is very close to a Gaussian distribution around zero ($\mu \approx 0.9^\circ$). The resulting mixed term $\sum \phi_i \cdot \delta\phi_j$, the separation between the dotted and dashed line in the top right panel, is close to zero.

It remains to evaluate the third term on the right hand side of equation (7), $\sum \delta\phi_i \cdot \delta\phi_j$, which is the small scale turbulent correlation. Whereas the mixed term extends over all scales, because it is a correction term due to a local turbulent fluctuation with any possible position angle in each scale range, the turbulent correlation is expected to extend over a spatially limited area, characterized by the turbulent correlation length. In Houde et al. (2009) this is taken into account by assuming a Gaussian window function where the width is the turbulent correlation length. In their further analysis the correlation length is then a fitting parameter. Here, we are directly making use of the turbulence statistical distribution to set a cut off in scale for the correlation term $\sum \delta\phi_i \cdot \delta\phi_j$. As in the case of $\sum \phi_i \cdot \phi_j$, the relevant quantity for the correlation is the difference, $\Delta = |\delta\phi_i - \delta\phi_j|$, between a pair of turbulence fluctuations $\delta\phi_i$ and $\delta\phi_j$. The distribution of Δ can again be constructed by calculating differences between two randomly chosen values from the distribution $\mathcal{D}(\delta\phi)$. $\mathcal{D}(\Delta)$ is shown for W51 (BIMA) in Figure 4, middle left panel, with a resulting mean difference in turbulence fluctuations $\mu_\Delta \approx 3.8^\circ$. We are adopting μ_Δ as a cut off measure. This means that $\delta\phi_i \cdot \delta\phi_j$ is counted as a correlation pair for a certain scale k if the difference in the corresponding $\phi_i \cdot \phi_j$ pair, $\Delta\phi = |\phi_i - \phi_j|$, is smaller than μ_Δ . Otherwise the correlation in $\phi_i \cdot \phi_j$

is considered to be dominated by the large-scale magnetic field. Alternatively, the cut off criteria can be refined by calculating the probability function of $\Delta\phi$ being of turbulent origin: to that purpose, the normalized distributions of $\mathcal{D}(\Delta)$ and $\mathcal{D}(\Delta\phi)$ are weighted against each other, Figure 4, bottom left panel. (When working with the normalized distributions, the weighting factors (see below) are not yet taken into account.) Comparing the distribution $\mathcal{D}(\Delta)$ with the distribution $\mathcal{D}(\Delta\phi)$ provides thus a tool to separate small and large-scale contributions. Both the μ_Δ cut off and the more sophisticated weighting with the probability function lead to very similar results. We therefore adopt the simpler criteria with μ_Δ in the following. Although $\mathcal{D}(\Delta)$ is only known in a statistical way, with the same μ_Δ used for each correlation pair, this average value can still be used to check against the measured difference in each correlation pair $\phi_i \cdot \phi_j$. Technically, we thus evaluate:

$$\delta\phi_i \cdot \delta\phi_j = \phi_i \cdot \phi_j \quad \text{if} \quad \Delta\phi \leq \mu_\Delta \quad (9)$$

When adding the two correlation parts in equation (7), $\sum \phi_i \cdot \phi_j$ and $\sum \delta\phi_i \cdot \delta\phi_j$, a proper normalization needs to be introduced. A factor $1/(N_k + N_{\delta,k})$ with $N_{\delta,k}$ counting the correlation pairs satisfying equation (9), normalizes the sum to one. The large-scale correlation function, $\langle \mathcal{C}_0 \rangle$, for each scale k can then be written as

$$\langle \mathcal{C}_0 \rangle_k = \frac{1}{N_k + N_{\delta,k}} \left(\sum_k \phi_i \cdot \phi_j + \sum_k \delta\phi_i \cdot \delta\phi_j \right) \quad (10)$$

with the condition in equation (9).

The isolated turbulent correlation, $1/N_{\delta,k} \cdot \sum \delta\phi_i \cdot \delta\phi_j$, is shown in Figure 4, middle right panel. A weighting factor $N_{\delta,k}/N_k$ is taken into account to directly compare its statistical significance with $\langle \mathcal{C} \rangle_k$ in the right upper most panel (weighting factor $N_k/N_k \equiv 1$). This additional weighting provides a spatial filter similar to assuming a Gaussian window function (Houde et al. 2009). It acts like a probability, for each scale k , that a measured $\Delta\phi \leq \mu_\Delta$ contributes to the turbulent correlation. We note that this is also valid when adopting the probability function as a cut off criteria, as mentioned above.

The bottom right panel in Figure 4 shows the final large-scale correlation function $\langle \mathcal{C}_0 \rangle_k$ by combining the upper two panels with the proper normalization from equation (10). Although the turbulent correlation shows a relatively sharp decrease over the smallest scales, its overall correction to $\langle \mathcal{C} \rangle_k$ (dashed line) is small. This is due to the small statistical significance (in terms of number counts) of the isolated turbulence differences in PAs. Adding up the various correlation factors with their statistical weight is one possible choice. Its most immediate advantage is that it gives directly the correct normalization.

Finally, we note that the characteristic large-scale polarization angle correlation length, λ_0 , is thus virtually unchanged compared to when it is directly calculated from the measured ensemble

of ϕ_i . From the middle panel, additionally, a turbulent polarization angle correlation length, λ_t , can be estimated in an analog manner.

REFERENCES

- Burkhart, B., Falceta-Gonçalves, D., Kowal, G., Lazarian, A. 2009, ApJ, 693, 250
- Chandrasekhar, S., & Fermi, E. 1953, ApJ, 118, 113
- Cho, J., Lazarian, A. 2005, ApJ, 631, 361
- Chrysostomou, A., Hough, J.J., Burton, M.G., & Tamura, M. 1994, MNRAS, 268, 325
- Chrysostomou, A., Aitken, D.K., Jenness, T., Davis, C.J., Hough, J.H., Curran, R., Tamura, M. 2002, A&A, 385, 1014
- Crutcher, R.M. 1999, ApJ, 520, 706
- Crutcher, R.M., Hakobian, N., & Troland, T.H. 2009, ApJ, 692, 844
- Curran, R.L., & Chrysostomou, A. 2007, MNRAS, 382, 699
- Dotson, J.L. 1996, ApJ, 470, 566
- Dotson, J.L., Davidson, J.A., Dowell, C.D., Schleuning, D.A., and Hildebrand, R.H. 2000, ApJS, 128, 335
- Dotson, J.L. et al. 2010, ApJS, 186, 406
- Draine, B.T., & Weingartner, J.C. 1996, ApJ, 470, 551
- Draine, B.T., & Weingartner, J.C. 1997, ApJ, 480, 633
- Falceta-Gonçalves, D., Lazarian, A., Kowal, G. 2008, ApJ, 679, 537
- Genzel, R., et al. 1981, ApJ, 247, 1039
- Girart, J.M., Rao, R., and Marrone, D.P. 2006, Science, 313, 812
- Goldreich, P., & Kylafis, N.D. 1981, ApJ, 243, 75
- Goldreich, P., & Kylafis, N.D. 1982, ApJ, 253, 606
- Goodman, A.A., Crutcher, R.M., Heiles, C., Myers, P.C., & Troland, T.H. 1989, ApJ, 338, L61

- Hildebrand, R.H., Davidson, J.A., Dotson, J.L., Dowell, C.D., Novak, G., & Vaillancourt, J.E. 2000, *PASP*, 112, 1215
- Hildebrand, R.H., Kirby, L., Dotson, J.L., Houde, M., Vaillancourt, J.E. 2009, *ApJ*, 696, 567
- Ho, P.T.P., Moran, J.M., and Lo, K.-Y. 2004, *ApJ*, 616, 1
- Houde, M., Dowell, C.D., Hildebrand, R.H., Dotson, J.L., Vaillancourt, J.E., Phillips, T.G., Peng, R., and Bastien, P. 2004, *ApJ*, 604, 717
- Houde, M. 2004, *ApJ*, 616, L111
- Houde, M., Vaillancourt, J.E., Hildebrand, R.H., Chitsazzadeh, S., and Kirby, L. 2009, *ApJ*, 706, 1504
- Kirby, L. 2009, *ApJ*, 694, 1056
- Lai, S.-P., Crutcher, R.M., Girart, J.M., Rao, R. 2001, *ApJ*, 561, 864L
- Lai, S.-P., Crutcher, R.M., Girart, J.M., Rao, R. 2002, *ApJ*, 566, 925
- Lazarian, A. 2000, *ASPC*, 215, 69
- Lazarian, A., Vishniac, E.T., and Cho, J. 2004, *ApJ*, 603, 180
- Lazarian, A., & Hoang, T. 2007, *MNRAS*, 378, 910
- Li, H., & Houde, M. 2008, *ApJ*, 677, 1151
- Li, H., Dowell, C.D., Goodman, A.A., Hildebrand, R.H., Novak, G. 2009, accepted by *ApJ*, arXiv:0908.1549
- Lunttila, T., Padoan, P., Juvela, M., Nordlund, Å. 2009, arXiv:0907.0587v1
- Matthews, B.C., McPhee, C.A., Fissel, L.M., Curran, R.L. 2009, *ApJS*, 182, 143
- Myers, P.C., & Goodman, A.A. 1991, *ApJ*, 373, 509
- Novak, G., Dotson, J.L., Li, H. 2009, 695, 1362
- Ostriker, E.C., Stone, J.M., & Gammie, C.F. 2001, *ApJ*, 546, 980
- Padoan, R., Jimenez, R., Juvela, M., Nordlund, Å. 2004, *ApJ*, 604, L49
- Rao, R., Crutcher, R.M., Plambeck, R.L., Wright, M.C.H. 1998, *ApJ*, 502, L75

- Rao, R., Girart, J.M., Marrone, D.P., Lai, S.-P., Schnee, S. 2009, ApJ, 707, 921
- Schleuning, D.A. 1998, ApJ, 493, 811
- Tang, Y.-W., Ho, P.T.P., Girart, J.M., Rao, R., Koch, P.M., Lai, S.-P. 2009a, ApJ, 695, 1399
- Tang, Y.-W., Ho, P.T.P., Koch, P.M., Girart, J.M., Lai, S.-P., Rao, R. 2009b, ApJ, 700, 251
- Tang, Y.-W., Ho, P.T.P., Koch, P.M., Rao, R. 2010, ApJ, 717, 1262
- Troland, T.H., & Crutcher, R.M. 2008, ApJ, 680, 457
- Vaillancourt, J.E. & Matthews, B.C. 2008a, in ASP Conf.Proc., Astronomical Polarimetry 2008: Science from Small to Large Telescopes, eds.P.Bastien & N.Manset, La Malbaie, Quebec, Canada
- Vaillancourt, J.E., Dowell, C.D., Hildebrand, R.H., Kirby, L., Krejny, M.M., Li, H., Novak, G., Houde, M., Shinnage, H., Attard, M. 2008b, ApJ, 679, L25
- Vallée, J.P., & Fiege, J.D. 2007, AJ, 134, 628

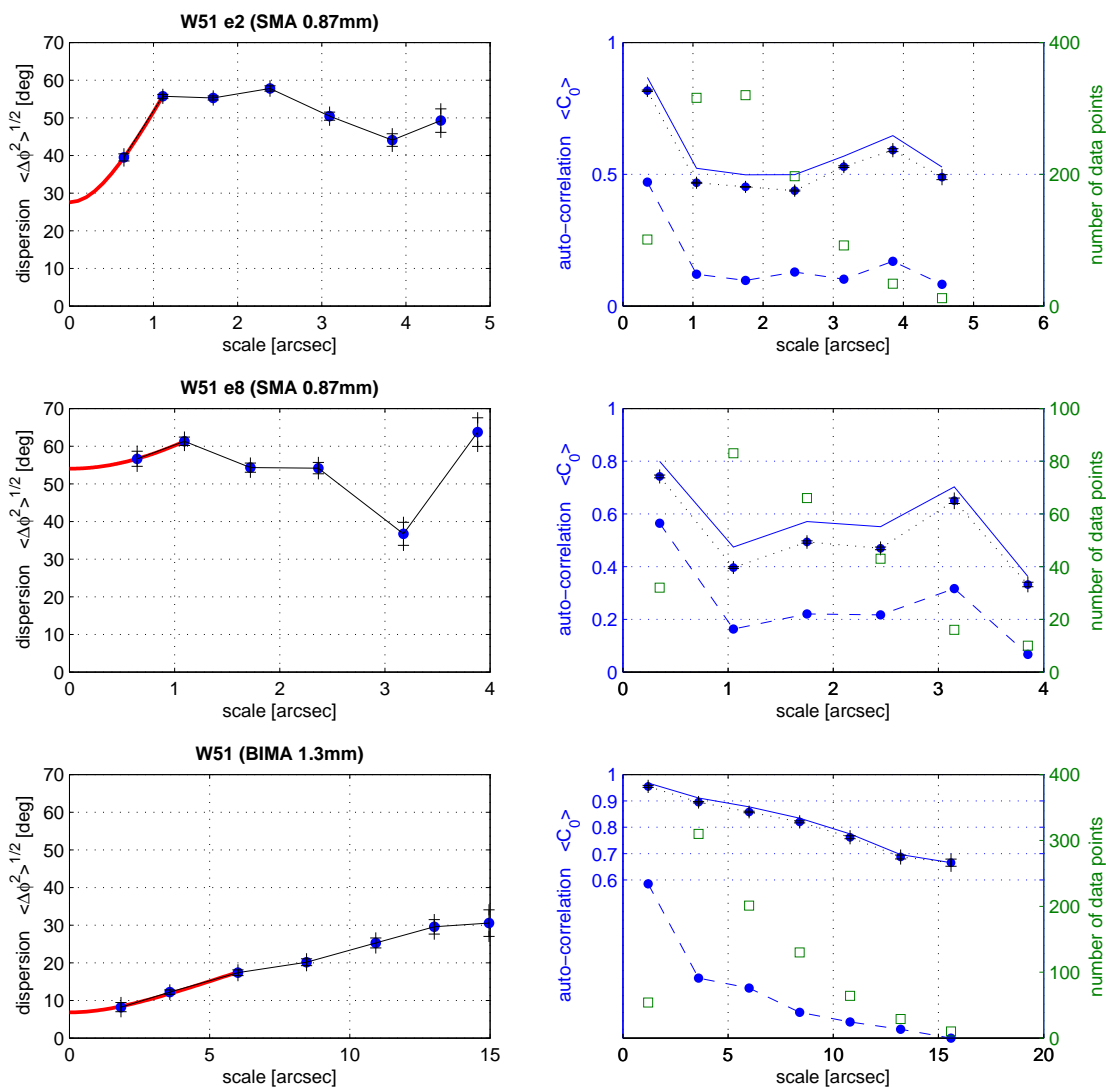


Fig. 1.— Left Panels: Dispersion (square root of second order structure function), binned to multiple integers of the resolution of each observation for W51 e2/e8. The assigned scale for each bin is obtained from averaging all the scales within a bin, which is very close to the synthesized beam in the first bin and close to the center for all the following bins. Correlated data points below the synthesized beam resolution are removed. Error bars are very small at the smallest scales due to the sample variance factor (large number of data points), and grow for the larger scales. The red line is the fitting result including the first two or three bins following equation (2), where the turbulent dispersion b is found from the interception of the fit at scale=0. Right Panels: large-scale polarization angle correlation function $\langle C_0 \rangle$ (solid line) binned to multiple integers of the resolution of each observation. The weighted integral of the curve measures the characteristic large-scale polarization angle correlation length λ_0 . The number of data points (pairs of PAs) within each bin is displayed (\square) with the axis on the right hand side of each panel. The same number of data points are also used for calculating the structure function, except where correlated data points are removed. Binned values are connected with straight segments for visual guidance only. The dashed line shows the turbulent polarization angle correlation function, separated by the method described in Appendix A. The dotted line is the raw auto-correlation function $\langle C \rangle$, directly derived from a measured ensemble of PAs without separating large and small scales. At the distance of W51 (~ 7 kpc), $1''$ corresponds to ~ 30 mpc ≈ 6190 AU.

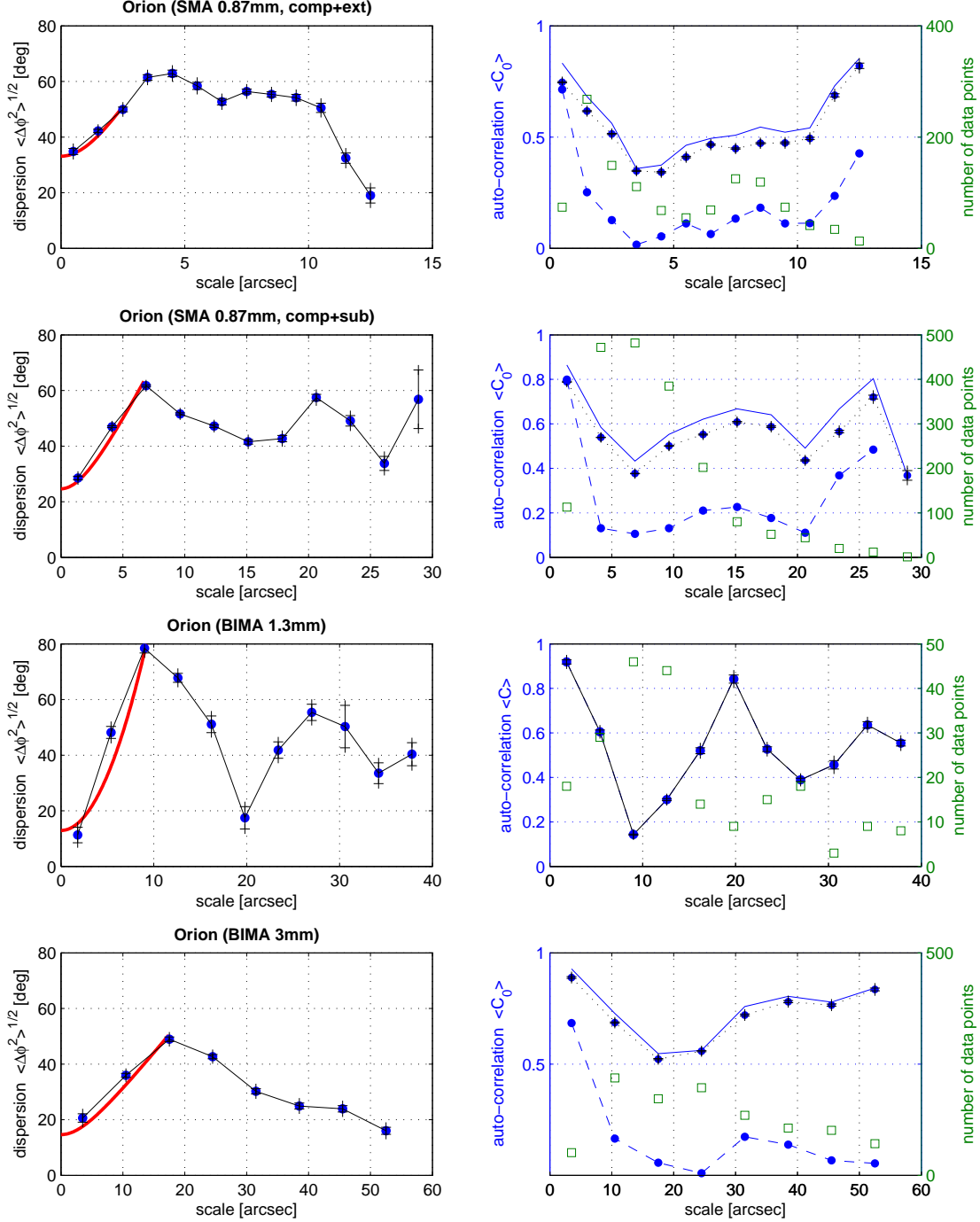


Fig. 2.— Identical to Figure 1, but for Orion BN/KL. No satisfactory solution was found for Orion (BIMA 1.3mm). The correlation shown is the raw polarization angle correlation function $\langle C \rangle$. At the distance of Orion (~ 480 pc), $1''$ corresponds to ~ 2.3 mpc ≈ 470 AU.

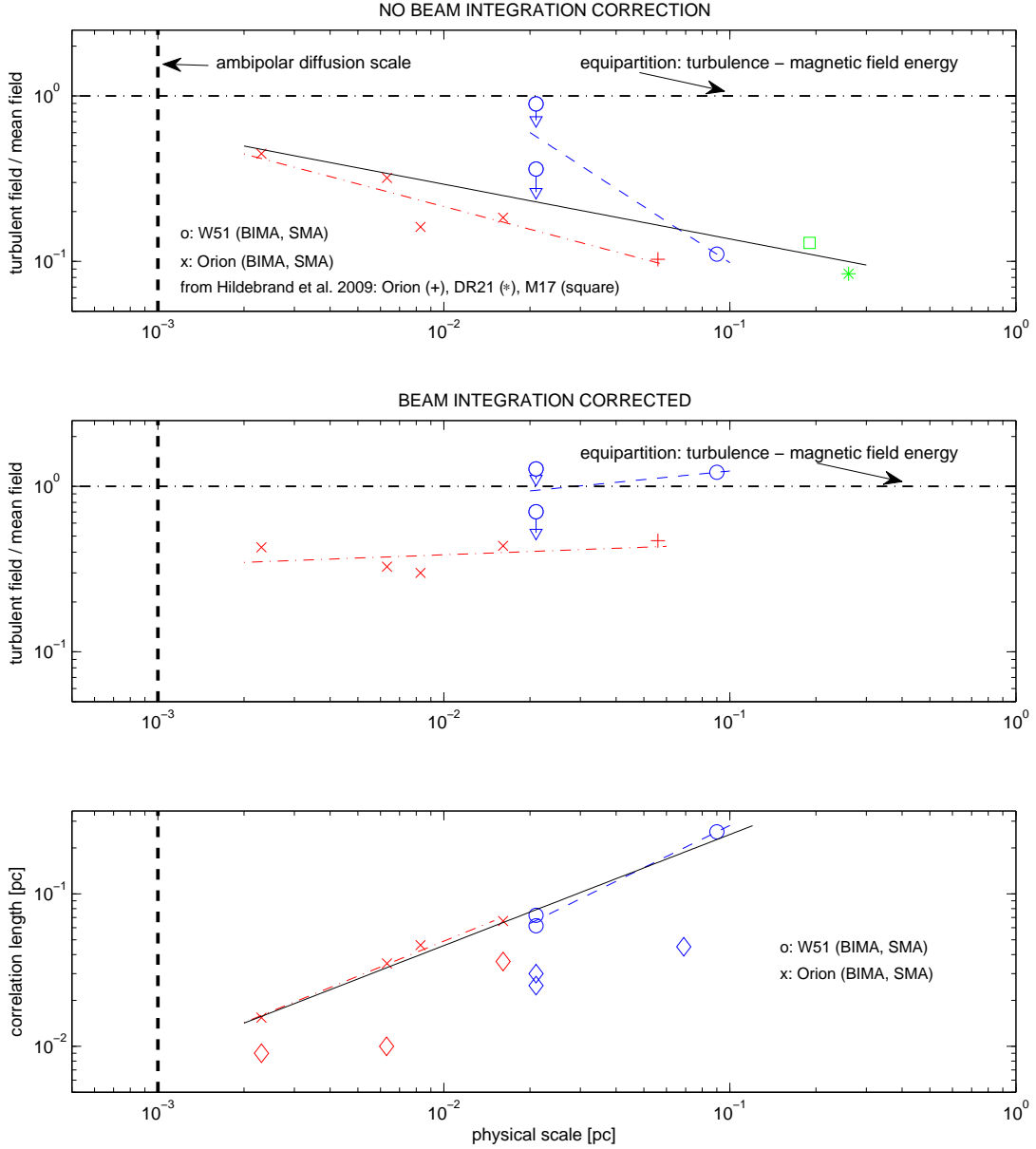


Fig. 3.— Top panel: turbulent to mean field strength ratio $\langle B_t^2 \rangle^{1/2} / B_0$ from various observations as a function of physical scale, as derived from the Figure 1 and 2. As relevant physical scale the achieved resolution (synthesized beam) at the source distance is assigned. Added to the BIMA and SMA data set are DR21 (*), M17 (\square) and Orion (+) from Hildebrand et al. (2009). The down arrows for W51 e8 and e2 mark the values after correcting for a possible gravity induced bias ($\sim -7^\circ$) as discussed in section 5.1. The middle panel shows the same ratio, but taking into account a beam integration correction as described in section 5.4. Resulting power law fits ($\propto l^\gamma$) in both panels are shown separately for the original W51 data (blue, dashed line), Orion (red, dot-dashed line) and the entire data set (black solid line, only top and bottom panel). The indexes are summarized in Table 2. For illustration shown is also the expected ambipolar diffusion scale at ~ 1 mpc from Li & Houde (2008) (dashed vertical line) and the turbulent - magnetic field strength equipartition line (dot-dashed line). Bottom panel: large-scale polarization angle correlation length, λ_0 , as a function of physical scale, together with the turbulent polarization angle correlation lengths (diamonds).

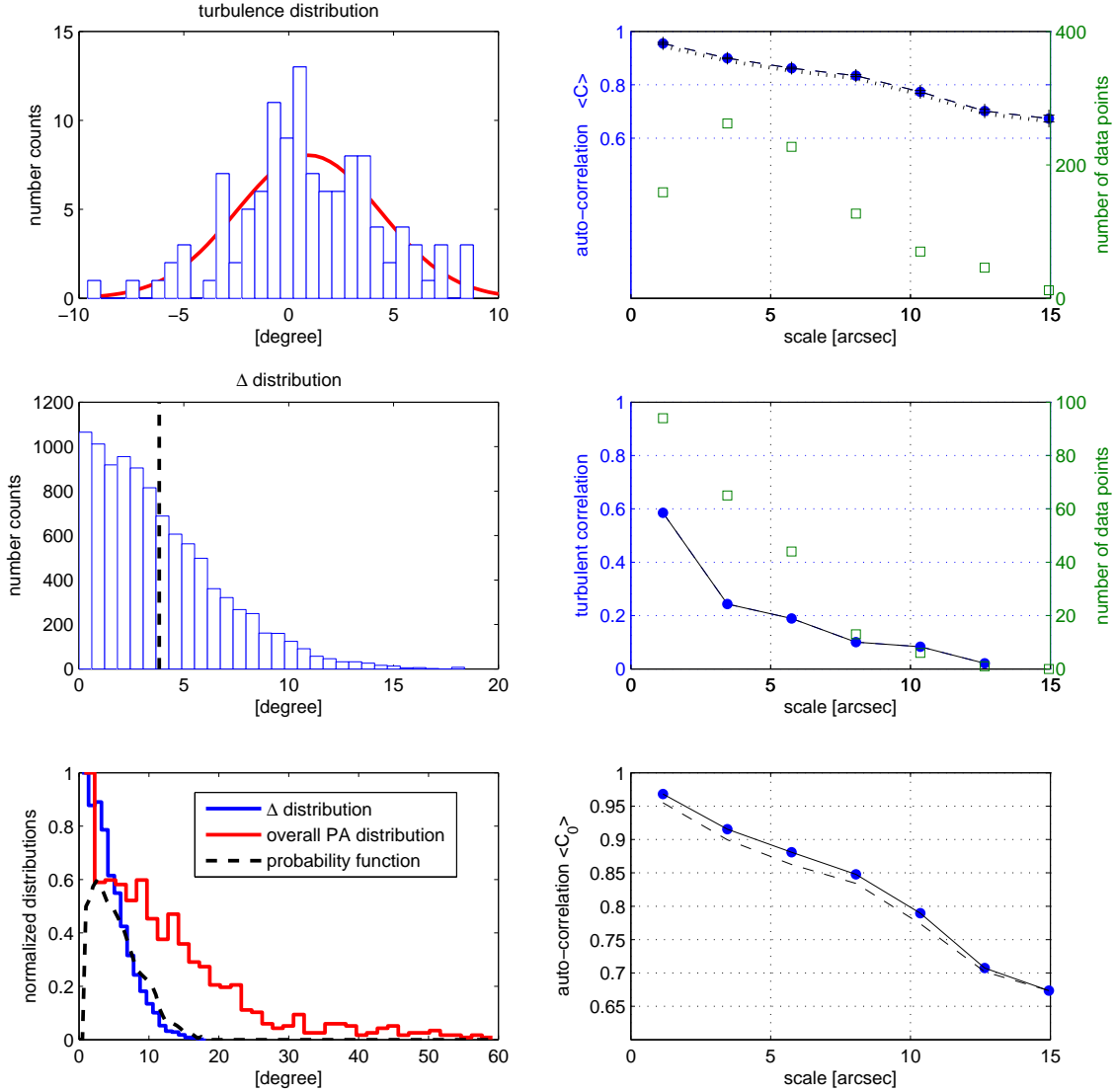


Fig. 4.— Illustration of the analysis of the polarization angle correlation function for W51, BIMA. Top left panel: the turbulence distribution $\mathcal{D}(\delta\phi)$, equation (8), with mean $\mu \approx 0.9$. The resulting correction to the raw auto-correlation $\langle C \rangle$ - ideally identical to zero for a Gaussian turbulence distribution around zero - is shown in the top right panel with the dotted line. The dashed line shows $\langle C \rangle$ calculated directly from the measured position angles ϕ_i .

Middle left panel: the distribution of differences between two turbulence values, $\mathcal{D}(\Delta)$, derived by random sampling two values from the distribution in the upper left panel. The larger number counts results from oversampling (calculating more difference pairs than combinations in $\mathcal{D}(\delta\phi)$). This also ensures a smooth distribution with a mean converging to $\mu_\Delta \approx 3.8$ (dashed line), which is used as a cut off criteria for the turbulent polarization angle correlation function (middle right panel). A statistical weight (number counts) is applied (see appendix). The large-scale auto-correlation $\langle C_0 \rangle$ (bottom right panel, solid line) is obtained by adding $\langle C \rangle$ and the turbulent correlation with the proper normalization from equation (10). The dashed line shows again $\langle C \rangle$ for comparison. The only small correction from the turbulent correlation results from its small statistical weight compared to the full distribution of differences in PAs which is used for $\langle C \rangle$. Bottom left panel: the normalized distributions of $\mathcal{D}(\Delta)$ (blue line) and $\mathcal{D}(\Delta\phi)$ (red line) which are used to derive the probability function (black dashed line) as an alternative to the cut off criteria in the middle left panel.

Table 1. Observation Summary and Results from the Statistical Analysis

Observation						Analysis							
instrument	λ	θ	θ	d	ref	b	$\frac{\langle B_T^2 \rangle^{1/2}}{B_0}$	m	α	λ_0	λ_r	N	$\left(\frac{\langle B_T^2 \rangle^{1/2}}{B_0} \right)_N$
	(mm)	($''$)	(mpc)	(mpc)	(5)	(deg)		(deg/ $''$)		(mpc)	(mpc)	(12)	(13)
	(1)	(2)	(3)	(4)		(6)	(7)	(8)	(9)	(10)	(11)	(12)	(13)
w51													
BIMA	1.3	2.3	69	300	I	6.4	0.08	2	1.1	230	45	122 ^d	1.22
SMA - e2	0.87	0.7	21	60	II	27.6 ^c	0.36	35	1.3	73	25	4 ^d	0.70
SMA - e8	0.87	0.7	21	60	II	54.0 ^c	0.89	10	0.3	63	30	4 ^d	1.27
Orion													
BIMA	3	7.0	16.1	69	III	14.6	0.18	3	1.6	66	36	6	0.44
BIMA	1.3	3.4	7.8	69	III	12.9	0.16	10	3.2	46	-	4	0.30
SMA ^a	0.87	2.8	6.4	23	IV	24.7	0.32	7	1.3	35	10	1	0.33
SMA ^b	0.87	0.9	2.1	23	IV	33.1	0.45	10	0.7	15	9	1	0.43

Note. — All statistical quantities are obtained from the Figures 1 and 2 with the method described in section 3.

⁽¹⁾observing wavelength

⁽²⁾synthesized beam resolution, also used as the separation in between the bins l_k ; for elliptical beams the geometrical mean is adopted, except for Orion BIMA 3mm where the semi-major axis is used because of its very elliptical beam

⁽³⁾synthesized beam in physical scale at source distance

⁽⁴⁾scale of variation in the large-scale polarization structure, empirically estimated from polarization maps by visual inspection

⁽⁵⁾references: (I) Lai et al. (2001), (II) Tang et al. (2009b), (III) Rao et al. (1998), (IV) Tang et al. (2010)

⁽⁶⁾turbulent magnetic field dispersion

⁽⁷⁾turbulent to mean field strength ratio

⁽⁸⁾slope over the first two bins (W51) or three bins (Orion) in the dispersion function $\langle \Delta \phi^2 \rangle^{1/2}$

⁽⁹⁾power law index of the second order structure function, $\langle \Delta \phi^2 \rangle \sim l^\alpha$, over the first two bins (W51) or three bins (Orion)

⁽¹⁰⁾plane of sky projected large-scale polarization angle correlation length

⁽¹¹⁾plane of sky projected turbulent polarization angle correlation length, derived from the method in Appendix A

⁽¹²⁾number of turbulent cells contained within telescope beam

⁽¹³⁾turbulent to mean field ratio corrected for beam integration effect

^acompact and subcompact observation combined

^bcompact and extended observation combined

^cpossibly influenced by gravity, with a bias of ~ -7 deg (section 5.1)

^dbased on approximating Δ' (effective depth of the molecular cloud along the line of sight) with the size of emission which is roughly the size of the maps in the SMA and BIMA observations. The turbulent correlation length δ is adopted from Houde et al. (2009).

Table 2. Power Law Indices γ for Scaling Relations

parameter	W51	Orion ^a	combined ^b
$\langle B_t^2 \rangle^{1/2} / B_0$ (uncorrected)	-1.51	-0.43	-0.33
$(\langle B_t^2 \rangle^{1/2} / B_0)_N$ (beam corrected)	0.17	0.07	–
λ_0	1.02	0.76	0.75

Note. — All power law indices γ are derived by fitting the relation $\propto l^\gamma$ as a function of physical scale l (Figure 3). Separate fits are performed to subsets (W51, Orion) and the entire data set.

^aincludes Orion from Hildebrand et al. (2009) for $\langle B_t^2 \rangle^{1/2} / B_0$ (uncorrected and beam corrected)

^bW51 and Orion combined. Orion, M17 and DR21 from Hildebrand et al. (2009) are included for $\langle B_t^2 \rangle^{1/2} / B_0$ (uncorrected). No joint fit is attempted with the beam corrected data. λ_0 is fit from the combined SMA and BIMA data, analyzed in the work here.